

Universal click-chemistry approach for the DNA functionalization of various nanoparticles

Nicole Siegel¹, Hiroaki Hasebe², Germán Chiarelli¹, Hiroshi Sugimoto², Minoru Fujii², Karol Kołataj^{1*}, Guillermo P Acuna¹

¹ Department of Physics, University of Fribourg, Chemin du Musée 3, Fribourg CH 1700, Switzerland

² Department of Electrical and Electronic Engineering, Graduate School of Engineering, Kobe University, Kobe 657-8501, Japan

*Corresponding author.

Email address: karol.kolataj@unifr.ch

Abstract

DNA conjugation is an important type of nanoparticle functionalization enabling a variety of applications. The reaction has been studied mainly for gold nanoparticles using thiolated DNA, which has resulted in many modifications of the method. A particularly useful scheme is the freeze-thaw process, which results in both a shorter reaction time and a higher surface density of DNA. However, the use of a thiol limits its application to noble metals only. In this work, we present that the freeze-thaw method can also be applied to the DBCO-azide click-chemistry reaction for the functionalization of various nanoparticles. Detailed studies of silica and silicon nanoparticles show that functionalization by freezing yields a 10-fold higher surface density of DNA compared to typical deposition methods. In addition, we used the obtained nanoparticles to synthesize new types of DNA origami nanoantennas to demonstrate their exemplary application. Finally, the method was used to successfully functionalize other nanomaterials, including oxides, polymers, core-shell, and metal nanostructures. Our results indicate that the presented method, in contrast to thiol functionalization, could become a new versatile and highly efficient scheme for DNA deposition on various nanoparticles.

Introduction

The field of colloidal nanotechnology has experienced continuous growth over the past few decades. It currently covers the whole spectrum of shapes and materials, such as metal, dielectric, oxide, carbon, magnetic and polymeric nanoparticles.^[1,2] Importantly, these kinds of nanomaterials display unique optical, electronic, magnetic, mechanical, physical and chemical properties that dissipate in bulk.^[3-8] However, all these nanoparticles are thermodynamically and energetically unfavorable relative to bulk materials, and even mild, physiological buffer conditions can induce aggregation.^[9-11] Therefore, to take full advantage of their properties, typically nanoparticles need to be further functionalized.^[12] Due to its unique specificity, addressability and biocompatibility, DNA is one of the most common choices for this purpose. Consequently, such nanoparticles have already found many applications in self-assembly, biosensor development, and drug delivery.^[13-18]

The first functionalization of nanoparticles with DNA has been presented in 1996 in the landmark paper of Mirkin et al.^[19] The method relies on a covalent binding of thiol-functionalized DNA to a metallic surface, and is still one of the most widely used functionalization approaches. As both the surface of the gold nanoparticles and the DNA strands are negatively charged, an effective means of repulsion screening is required for efficient functionalization.^[20] Typically, this is realized by high salt concentration in a process known as ‘salt aging’.¹⁷⁻¹⁹ However, even low salt concentration can induce aggregation.¹⁹ Therefore, salt has to be added very slowly, making the whole method highly time-consuming. Recently, many new methods have been developed to reduce the functionalization times

using either chemical (acids, surfactants, organic solvents) or physical means (microwaving and freezing).^[21–25] Among these, freezing is particularly well-suited because it does not introduce any additional chemicals, nor involves elevated temperatures, which could affect the nanoparticles. The increase in the DNA deposition is achieved by concentrating both nanoparticles and DNA strands during freezing process. In this way, not only can the reaction time be reduced to around 1 hour, but the deposition density can also be significantly improved compared to ‘salt aging’ method.^[25]

In general, the described methods provide, a reliable way to functionalize noble and coinage metals.^[26–28] Nevertheless, it relies on the high affinity between thiols and the metallic surface, which has, until now, served as a barrier for exploring the fundamental properties of different nanomaterials.^[29] Namely, the reaction cannot be used for nanoparticles with a surface composition that is inert to thiols, including oxides, core-shell and polymeric nanoparticles, and even nanoparticles composed of active metals (Al, Ga) and metalloids (Si, Ge). Importantly, they exhibit various and unique physicochemical properties, which find a wide range of practical applications.^[30–36] Silicon nanoparticles (SiNPs) are an interesting example of nanoparticles that cannot be functionalized using thiol chemistry. These high refractive index dielectric nanoparticles have received a lot of attention in recent years, due to their low heat losses and strong magnetic and electric modes.^[36] These features of Si NPs leads to their potential applications in chiral sensing, unidirectional scattering, and the manipulation of magnetic dipole transitions.^[37–42] Importantly, described properties are unique for this class of nanoparticles making them a convenient alternative for plasmonic nanoparticles, which exhibit relatively high losses and the absence of magnetic response at optical frequencies.^[36]

Given the amount and importance of nanoparticles that cannot be decorated with DNA using thiol chemistry, the need to find an efficient, low-cost, and rapid method of functionalization is obvious. Recently, a click chemistry reaction called strain-promoted alkyne azide cycloaddition (SPAAC), has been increasingly used for this purpose.^[43–46] Not only does it demonstrate very high specificity, where DBCO only reacts with azide groups, but it also works in both aqueous and organic solutions and does not require elevated temperatures, extreme pH conditions or high salt concentrations. Furthermore, the reaction is not material-specific, and can be applied to any type of nanoparticle, as long as the azide is present on its surface.^[47,48] Similar to thiol functionalization, also in this case repulsion between nanoparticles and DNA strands can diminish the final DNA surface density and extend the entire process to at least one day. This feature can be particularly limiting for biological applications where nanoparticle stability plays a key role. However, very little attention has been paid on trying to solve this problem in the SPAAC reaction, with only one report on the application of salt aging method in this process.^[46]

Inspired by the recent developments in the functionalization of Au nanoparticles, we report a novel approach to conjugate DNA on various nanomaterials by employing freezing assisted SPAAC, with the special focus on the functionalization of Si and SiO₂ NPs. Impressively, this very simple method of functionalization proved to have a tremendous effect on the overall deposition efficiency. To support this statement, we compared it with different approaches used for the DNA functionalization with SPAAC. Not only freezing reduces reaction times but it also significantly increases the concentration of DNA on the nanoparticles rendering them stable in various conditions. Significantly, we successfully applied this method for the conjugation of DNA on silicon nanoparticles. To the best of our knowledge this is the first report of stable DNA-functionalized Si nanostructures, which opens up their various applications in optics and sensing. As an exemplary application, we employed the DNA origami technique, which has been extensively employed to design nanoantennas with plasmonic nanostructures, to fabricate constructs with arbitrarily positioned Si and SiO₂ nanoparticles. Finally, we present the versatility of this method by realizing the DNA functionalization of different nanoparticles: oxide – TiO₂, Au@SiO₂, polymeric – PMMA and PS, as well as metallic nanoparticles – Au.

Results and discussion

DNA functionalization of SiO₂ and Si NPs

SiO₂ NPs are well studied, widely available and easy to produce. Moreover, the oxide-rich surface allows the use of silane chemistry to decorate the NPs with azide for further DNA functionalization via SPAAC (Figure 1). Therefore, these particles are an excellent reference point for a thorough investigation of the freezing process. On the other hand, Si NPs present new optical properties and can replace gold as a material for specific applications in light detection and manipulation. However, an efficient method for coating them with DNA is still lacking. Significantly, Si NPs naturally formed an oxide layer that provides them stability, so the results obtained for our benchmark SiO₂ nanoparticles should be easily translated to silicon.

Figure 1 illustrates the general protocol for DNA functionalization of SiO₂ and Si NPs. The process begins by reaction with a chloride-terminated silane (CPTMS), followed by chloride to azide substitution (Materials and methods), (Figure 1A). The successful deposition was confirmed colorimetrically by the reaction with DBCO-Cy5 and Cy7, in which the nanoparticles changed color due to the presence of fluorophores (Figure 2A, Figure S 1A). As the surface density of azide determines further efficiency of the DNA functionalization, we started by optimizing the deposition of the aforementioned groups. The surface density was quantified by extinction at 650nm (Figure S1a) after the freezing-assisted reaction between SiO₂ NPs and DBCO-modified Cy5 (equation S1). In this regard, one can assume that freezing could induce unspecific binding of molecules to the nanoparticles surface.^[49,50] Therefore, to evaluate the quantification method, we additionally carried out the reaction with non- and chloride terminated NPs as reference. Obtained results confirm that freezing does not change the reaction specificity and only azide-functionalized SiO₂ (SiO₂-N₃) nanostructures exhibit the color of Cy5 molecules (Figure S1). Initially, the different reaction ratios were tested observing that an increase of CPTMS excess, up to 10³-10⁴/nm², led to greater surface coverage with a sharp drop at the ratio of 10⁵/nm². We attribute this to the cross-bonding between the nanoparticles, which was supported by DLS measurements displaying aggregation of both SiO₂ and Si structures under these conditions (Figure S1C, Figure S5A). Furthermore, we carried out kinetics study of the reaction for the ratio yielding the highest deposition, i.e. 10³/nm², observing the saturation of the surface at 0.85Cy5/nm².

In the next step, deposited DNA on the nanoparticles using a click chemistry, SPAAC, reaction based on a stable triazole bond between DBCO and azide molecules (Figure 1). In this regard, we adapted the technique taking advantage of the local concentration of both nanoparticles and DBCO-DNA molecules in liquid pockets during freezing to significantly increase the deposition efficiency (Figure 1A). Figure 2 A presents a photo of thawed colloidal Si NPs after the freezing reaction with an excess of DBCO-T22 (sequence of 22 thymines) DNA strands. Noticeably, the bare nanoparticles aggregate during the reaction and the colloid loses its color, while the Si-N₃ NPs remain stable. The difference in stability is clearly visible in DLS measurements, where the hydrodynamic radius of bare Si nanoparticles increases significantly, while no substantial change is observed for azide-decorated structures after the freezing reaction (Figure S5 A). We assume that Si-N₃ NPs maintain stability during freezing due to deposition of the DNA layer, protecting it from aggregation. This hypothesis is supported by our further measurements, where we compared the stability of Si-N₃ NPs at various pH conditions before and after the freezing reaction with DBCO-T22. The results demonstrate that the nanoparticles indeed gain increased stability after the functionalization process and no significant change in hydrodynamic radius is observed up to pH 10, whereas Si-N₃ which did not undergo the reaction tends to aggregate at low pH due to surface protonation. Furthermore, we measured the zeta potential of the nanoparticles before and after the freezing reaction, observing the general trend of the surface potential decrease due to the deposition of negatively charged DNA (Figure S5 B). The lowest values of -37 eV were measured for the reaction ratio of CPTMS/surface of 10²-10³/nm² indicating the most efficient DNA conjugation for these conditions. These results were later supported by the gel electrophoresis, showing the highest stability and electrophoretic mobility of Si-T22 NPs in these conditions (Figure S5 B, C).

Subsequently, we conducted electron energy loss spectroscopy measurements of 140 nm Si nanoparticle grafted with DBCO-T36 to investigate the morphology of the nanoparticles after the DNA deposition (Figure 2 B). The micrographs present the TEM-EELS measurements with the elemental analysis, where we could observe the overlap of the signal of oxygen and phosphorus on the nanoparticle

surface, further indicating the presence of DNA. As the ultimate proof of high surface coverage, we performed CryoEM measurements of T36 grafted NPs (Figure 2 C), (Figure S5 D). Obtained results confirm the existence of a 10.5 nm homogenous DNA shell on the nanoparticles surface, which is consistent with the expected values for such DNA length.^[51,52]

Based on the results, we can prove an effective process of coating Si-N₃ NPs with a DNA layer. However, high extinction coefficient of Si NPs conceals the absorption signal of DNA, limiting any quantitative studies. Therefore, to assess the amount of DNA on the surface we studied the reaction with SiO₂ nanostructures instead. For this, the nanoparticles were functionalized with DBCO-T22 and the deposition was quantified by extinction at 260nm, showing the gradual increase of surface density up to 0.2 DNA/nm² for the reaction ratio of 10⁴ CPTMS/nm² (Figure S2 B). The decrease in surface density between DBCO-Cy5 and DBCO-T22 from 0.85 to 0.2 molecules/nm² can be explained by the repulsion of negatively charged DNA on the surface, reducing the overall efficiency of the SPAAC reaction. Nevertheless, this concentration appeared to be sufficient to maintain the stability of the nanoparticles and allow them to be applied to the gel for electrophoresis (Figure S2 A). As with DBCO-Cy5, the reaction can be also explained by non-specific DNA binding to the surface, which has been already observed for gold nanoparticles^[49]. To verify it, we tested the DBCO-T22 deposition on bare and chloride-functionalized nanostructures (SiO₂-Cl) (Figure S2 A). The absence of a DNA peak at 260 nm for SiO₂ and SiO₂-Cl signified that the process is based on the reaction between DBCO and azide groups, rather than non-specific adsorption on the surface.

The DNA functionalization of nanoparticles cannot be considered as a simple reaction between two reactants (thiol-gold, DBCO-azide), as it is influenced by other parameters, for example an interaction between the DNA sequence with the nanoparticles surface. This sequence dependence, for example, has been well characterized for gold nanoparticles, where a thymine-rich sequence yields significantly higher surface densities than other nucleotides. We wondered whether, for the studied nanoparticles, the conjugation efficiency also depends on the DNA sequence involved. To examine it, we carried out the freezing reaction with DBCO-modified poly T (T18), poly A (A18), poly C (C18), poly G (G18), and random sequence (CTTCTCTACCACCTACAT). The amount of DNA conjugated to SiO₂ NPs was calculated quantitatively using previously described spectral method. Moreover, to get the information about the deposition efficiency of Si NPs, we assess the relative surface density instead. The method is based on the relationship between the DNA surface concentration and the stability of nanoparticles in high salt concentration (Figure 3 A).^[53] Basically, the more DNA on the surface, the higher the stability of the colloid. Our results indicate that indeed the binding efficiency of the studied reaction strongly depends on the sequence involved with highest surface density obtained for G18, followed by T18, R18, A 18 and C18 (Figure S3 A). This trend is also observed in the higher stability of densely functionalized nanoparticles, except nanostructures decorated with G18 sequence (Figure 3 B, Figure S3 B/C). We hypothesize that the disproportionately low stability of the G18-functionalized nanoparticles may be related to the formation of G-quadruplexes connecting the nanoparticles^[54] together. The results of the functionalization with C18 sequence are particularly interesting, as it is the only sequence binding unspecifically to the surface (Figure S3). It can be connected to a high affinity of cytosine to nanoparticles surface, resulting in wrapping the nanoparticle with this sequence. This process has been already observed for adenine and cytosine-rich sequences for gold and silver nanoparticles respectively.^[49,55] Overall, the unspecific adsorption of the sequence to the nanoparticle surface reduces the deposition density and the stability of nanostructures, which is consistent with obtained results (Figure 3B, Figure S3B).

As discussed before, the use of SPAAC in nanotechnology is not new itself and it has been already employed as the mean to conjugate DNA on the surface of various entities, including SiO₂ nanostructures. Therefore, we wondered if the freezing process would actually increase the grafting efficiency, as it is in case of thiol functionalization of gold nanoparticles. For this, we compared freezing assisted deposition with already reported SPAAC protocols such as room temperature mixing for 48 hours or salt aging^[43,46]. Our quantitative measurements of DNA (T22) deposition on SiO₂ nanostructures indicate that, also for SPAAC, freezing substantially increases the amount of conjugated DNA from 0.01 and 0.07 DNA/nm² for the mixing and salt aging method respectively to approximately 0.13-0.16 DNA/nm² for the freeze-and-thaw process (Figure S4 A, B). Consequently, the elevated DNA surface density leads to increased stability of nanoparticles at high salt concentrations, where, in contrast

to other tested protocols, no significant aggregation up to 20 mM MgCl₂ is observed using freeze and thaw method (Figure S4 C). The difference between efficiency of tested deposition methods was particularly evident in case of Si NPs (Figure 3D). In general, Si NPs are considerably less stable than SiO₂ nanostructures and easily aggregate in high salt concentration. This is clearly visible through the partial aggregation of the nanoparticles and the loss of color of the colloid during salt aging functionalization, while they sustain colloidal stability with other methods (Figure 3D). One could wonder why Si NPs do not show signs of aggregation during the freezing process, which is also based on the increase of local salt concentration. However, these results should not surprise, as the freezing process takes around one hour in total, probably the actual formation of liquid pockets during phase transition is much faster. Therefore, the nanoparticles are just briefly exposed to high salt concentration before DNA deposition occurs, reducing aggregation compared to salt aging. These results, clearly show that even though salt aging yields reasonable DNA conjugation, which was presented for SiO₂ NPs, the method has its limitations for nanostructures presenting low colloidal stability. Furthermore, in order to compare different deposition methods, we dispersed Si NPs functionalized DNA under unfavorable conditions such as high pH and high salt concentration (Figure 3D). The results confirm that the freezing method provides the highest DNA deposition, protecting the nanoparticles from degradation in pH 12 and 1M NaCl solutions, while other nanoparticles already aggregate after only 10 minutes under these conditions. The difference in stability was also observed on the electrophoresis gel, where only the freezing method resulted in the necessary DNA density allowing them to run on a gel (Figure 3E). Interestingly, we were able to further decrease the size dispersion of Si NPs, from 15% in the sucrose gradient to about 6% after running them on an agarose gel (Figure 3 E,F, Figure S6). Considering that many of the optical properties of nanoparticles depend on their size,^[3,56] we see the possibility to fractionate nanostructures by gel electrophoresis as an important advantage of the freezing method, which is not offered by other tested procedures.

Si nanoantennas assembly with DNA Origami

As already emphasized, the colloidal stability of nanoparticles is a prerequisite for their applications in sensing, drug delivery, and self-organization. Nanoparticle-enhanced sensing is one of their most important applications as they can strongly enhance the signal of studied molecules, enabling down to a single-molecule detection.^[57-59] One of the most useful techniques used for this purpose is the DNA origami method. The DNA origami is a bottom-up method based on the self-assembly of DNA strands into arbitrarily designed 3D structures. Due to the high addressability and specificity of the building blocks - the oligonucleotides - the DNA origami technique is an excellent template for assembling different entities, such as fluorophores, proteins, or nanoparticles. Consequently, it has been widely used to produce a variety of nanoantennas for sensing and light manipulation. However, the binding of nanoparticles to DNA origami is usually carried out in salt buffers, which limits its application only to nanoparticles stable under these conditions. Hence, the nanoantennas obtained by this method have so far used Au, Ag and QD nanoparticles. Therefore, given the optical properties of Si nanoparticles and encouraged by our results of the DNA deposition, we decided to focus our efforts on the fabrication of the types of Si, and our benchmark SiO₂, DNA origami nanoantennas.

For this end, we used a long frame-work of DNA origami comprised of 12 helix bundle with a final length of 180 nm and a 20 nm pedestal in the middle (Figure S8A). To realise the binding of the nanoparticles to DNA origami, two lines of poly adenin handles were protruding from either one (1 BS) or two sides (2 BS) of the pedestal (Figure S8A) allowing the complementary attachment of one or two nanoparticles accordingly. Overall, 16 handles of 8 adenines (8A) each were used to bind one nanoparticle. Additionally, a single DNA strand of the DNA origami structure was modified with an Atto647N fluorophore for the surface detection using wide-field microscopy, and with biotin molecules for biotin-neutravidin surface binding.

The fabrication of DNA origami nanoantennas, was achieved by following the protocols known from the assembly of gold and silver nanoparticles. To synthesize nanoantennas in this work, we used either 100 or 150 nm SiO₂, or one of two sizes (120 and 150 nm) of Si NPs. The protocol described below is a generic approach for the binding of Si and SiO₂ to DNA origami that has been used for all studied nanoparticles without further modifications. Firstly, we realised the functionalization of Si NPs

using 1:1 ratio of T18/28 DNA with freezing method. A mix of long (T28) and short (T18) staples was rationally employed in the nanostructures functionalization to obtain a DNA shell with well separated long strands. It allows enough space for the complementary strands on nanoparticles and DNA origami to hybridize efficiently. Following, the DNA-functionalized nanoparticles were purified from an excess of DNA strands by gel electrophoresis (Figure 4B), (Figure S X 9– SiO₂ gel). Afterwards, purified nanoparticles were arranged on DNA origami structures by DNA hybridization (Figure 4A). Obtained nanoantennas were subsequently purified by gel electrophoresis from an excess of nanoparticles and aggregates (Figure 4B, Figure S9). The appearance of additional bands after the reaction indicates the successful formation of DNA origami nanoantennas. However, whereas the additional bands are clearly visible in case of SiO₂ nanostructures, the smearing of Si nanoparticles makes detecting them more difficult. We pair it with size dispersion of Si NPs, resulting in different gel electromobility. Moreover, we observed that both Si and SiO₂ NPs themselves tend to create intrinsic dimers even without DNA origami, further impeding analysis of the gel.

Therefore, to confirm the attachment of Si and SiO₂ NPs to DNA origami structures, we decided to use a method based on colocalization of the fluorescence signal with scanning electron microscopy (SEM). First, the nanostructures obtained after binding, were deposited on glass substrates with grids and the fluorescence measurements were carried out using widefield microscope (WF). Thereby, the position of DNA origami structures containing Atto 647N molecules was determined. Then, to assess the origin of the fluorescence signal, the morphology of the deposited substrates was investigated using SEM. Figure 4 C and D present an exemplary WF and SEM measurements of the structures obtained after binding 150 nm Si NPs to DNA origami containing two binding sides (2BS). The measurements confirm the binding of Si nanoparticles to DNA origami structures, as they show the colocalization of the Atto 647N fluorescence signal with the position of the nanoparticles in the same area of the glass sample. To confirm that the nanoparticle binding is specific and can be controlled by the DNA origami design, we performed a self-assembly process using structures dedicated to obtain either the monomer (1 BS) and dimer (2 BS). We observed that the amount DNA origami-mediated of monomers and dimers depends on the structure used for binding (Figure S 8C). For the 1 BS design, 88.2, 66.7, and 88.6% of the localised nanostructures were monomers, and dimers accounted for 11.8, 21.7 or 11.4%, for 150 nm Si, 120 nm Si, and 150 nm SiO₂ respectively. On the other hand when 2 BS DNA origami was used, the samples contained only 24, 30.4, and 71% of monomers and 76, 54.3, and 29% of dimers. This results confirm that the binding between NPs and DNA origami is specific and dependent on the number of binding sites in the design. In this context, it should be emphasized that probably not all of dimers that we observe come from binding of two monomers to DNA origami with 2 BS. This is due to the self-dimerisation of the nanoparticles after azide and DNA deposition, and these dimers account for around 10-20% of all structures, depending on the used nanoparticles. Therefore, obtained dimers can come either from desired binding of two monomers to DNA origami or from intrinsic dimers binding to one binding side (Figure S 8B). This process can also explain relatively high amount of dimers in samples dedicated for monomers (Figure S 8C).

Versatility of freezing-assisted SPAAC DNA deposition

The presented results of Si and SiO₂ functionalization clearly show that the use of freezing in SPAAC reaction increases the DNA deposition efficiency and renders nanoparticles stable in high salt concentration. Also, it has been already presented that the SPAAC reaction can be used for the functionalization of other nanoparticles decorated with azide groups. In this context, one can ask if it is possible to employ the same freezing approach for other nanostructure or maybe this method is specific only to Si and SiO₂ nanoparticles. To answer this question, we decided to explore the versatility of the protocol for the DNA functionalization of different nanoparticles.

In all studied cases, we followed the same protocol known from the functionalization of our benchmark, SiO₂ NPS. In general, we start with the azide deposition, unless it is already present on the surface, followed by the freezing-mediated DNA functionalization (see Materials and Methods).

Furthermore, as we tested the method for nanoparticles with different sizes and physico-chemical properties, we employed different ways to confirm the realisation of the DNA functionalization.

The most reasonable starting point for our analysis is the functionalization of other hydroxyl-rich nanoparticles, which, due to oxide groups on the surface, should present similar surface chemistry to SiO₂ NPs. We firstly attempted the DNA functionalization of Au@SiO₂, which is an interesting example of nanoparticles with hydroxyl-rich surface as it is build of metallic core and oxide layer (Figure 5A). The core is typically of the main interest due to gold plasmon resonance, and the shell protects the structure from the environment. However, the nanoparticles cannot be easily functionalized with thiol-DNA as it is in case of Au NPs, due to inert silica shell. Therefore, even a thin silica layer limits many of their applications, for example for previously presented DNA origami optical nanoantennas. Yet, for our freezing method this is the easiest case to consider as it has the same surface as SiO₂ nanoparticles. Indeed, Au@SiO₂ showed a successful DNA functionalization with DBCO-T36, remaining stable towards high salt concentrations (Figure S 10A) and running through an agarose gel (Figure 5A). Other oxide nanostructures of high interest that could be functionalized with our method are TiO₂ NPs. Firstly, the functionalization with N₃ groups was confirmed colorimetrically by the reaction with DBCO-Cy7 (Figure 5B). Further, the same approach was used to study the freezing-mediated DNA conjugation. For this, we used modified DBCO-T18 DNA with additional, single Cy3 molecule. Distinct pink colour of the fluorophore was only observed for TiO₂-N₃ while bare nanoparticles remain white after the reaction, confirming the specific deposition of DBCO-T18-Cy3 on the surface of TiO₂-N₃ NPs. Functionalisation of the nanoparticles by DNA was also evident in their increased stability under high salt concentration (Figure S 10B).

Afterwards, in order to increase the spectrum of explored structures, we investigated the possibility of applying our method to the functionalization of commercially available N₃-functionalized polymeric particles. To this end, we decided to focus our attempts on two types of broadly used 2 μm PMMA@N₃ and 5 μm PS@N₃ microspheres. The amorphous character of these particles can often lead to physisorption of various molecules. Therefore to assess the binding of DNA to their surface we carried out the reaction with Cy3-modified DNA sequence with and without DBCO. Emission spectra and images of nanoparticles show that indeed some physisorption of R50-Cy3 is observed during freezing, however the reaction with DBCO-R18-Cy3 yields 12 and 6.7 times higher grafting density for PMMA and PS particles respectively (Figure 5C, Figure S 10C,D).

As a final test of the versatility of our method, we decided to extend our considerations to another important class of nanostructures - metallic nanoparticles. In terms of usefulness and scientific interest, gold nanoparticles represent the most important representative of this type of nanostructures therefore we selected them as the object of further studies (Figure 5D). Firstly, bare Au NPs were decorated with N₃ group via the reaction with SH-PEG5-N₃, followed by the freezing-mediated functionalization with DBCO-T18. To eliminate the influence of unspecific binding, we carried out the reaction with both azide-functionalized and bare Au NPs. The difference between these nanoparticles after freezing is clearly visible using gel electrophoresis, in which only azide-decorated Au NPs move through the gel, while bare ones aggregate in the gel pocket. These results indicate the DNA functionalization of also this type of nanoparticles can be successfully realised using our freezing method.

Conclusions

In conclusion, inspired by recent advances in DNA deposition on AuNPs and motivated by the lack of a universal and reliable method to functionalize other nanoparticles, we used freezing assisted SPAAC to deposit DNA on a variety of nanoparticles. We chose silicon and silica nanoparticles as the reference point and the most important object of our research. Tests carried out on these nanoparticles have proven that the freezing method can be successfully applied to their functionalization with DNA molecules. The results indicate that this method not only shortens the reaction time from about two days for typically reported SPAAC methods to an hour, but also increases the density of the DNA cover by

more than 10 times. Compared to other methods, the obtained nanoparticles also showed excellent colloidal stability, promising their new applications in various fields. As a proof of concept, we used the obtained nanostructures to fabricate Si and SiO₂ nanoantennas with well-established nanotechnology technique called DNA origami. According to our knowledge, this is the first report of the use of Si and SiO₂ NPs in this method. This is particularly important for Si nanoparticles exhibiting unique optical properties not presented for typically used plasmonic nanoparticles. Finally, we have applied the method to the functionalization of other nanoparticles: oxides (TiO₂), core-shells (Au@SiO₂), polymers (PMMA, PS) and metals (Au), demonstrating the versatility of our process. We believe that this method can become a universal method for DNA functionalization of different nanoparticles, opening new possibilities for their application in biosensing, drug delivery and self-assembly.

Materials and Methods

Materials. Methanol $\geq 99\%$ (MeOH), Ethanol $\geq 99\%$ (EtOH), and 99.8%, Extra Dry, AcroSeal™ Dimethylformamide (DMF), and NeutrAvidin Protein were purchased from Thermo scientific; 97% 3-Chloropropyltrimetoxysilane (CPTMS), phosphate buffered saline pH7.5 10x (PBS), Tris acetate EDTA buffer 50X pH 8.0 (TAE), and Magnesium chloride 1M (MgCl₂), and DBCO-Cy7 were purchased from Alfa Aesar; Dimethylamine (DMA), Ammonia solution 28–30% (NH₄OH), Sodium azide (NaN₃), 10% Sodium dodecyl sulfate (SDS), Tetraethyl orthosilicate (TEOS), Albumin biotin labeled bovine, 16-mercaptohexadecanoic acid (MHA), and DBCO-Cy5 were purchased from Sigma Aldrich. Thiol-dPEG5-azido (SH-PEG5-N₃) was purchased from Biosynth.

Nanoparticles.

Silica. 150nm Silica nanoparticles were prepared by Ströber method^[60] 285ml Ethanol, 40ml milliQ water, and 6.4 ml NH₄OH were added to a 500 ml flask with a stopper and magnetic stirred at 350 rpm at 30°C for 20min. 12ml of TEOS were incorporated rapidly to the mixed and reacted for 3h. NPs were purified by centrifugation at 5000rpm for 5min and resuspension twice in methanol and twice in water consecutively. SiO₂ NPs were dried overnight on a desiccator, for further functionalization with azide.

Silicon. Crystalline silicon nanoparticles (Si NPs) were prepared by thermal disproportionation (1450 °C) of commercially available Silicon monoxide (FUJIFILM WAKO) in N₂ atmosphere for 30 min. Si NPs were liberated from Silicon dioxide matrices by etching in HF solution (46 wt%) for 1 h, transferred to methanol and ultrasonicated for 1min. The NPs were size separated by sucrose gradient centrifugation process. First, we added sucrose solution with different concentration (35-45 wt%) to a centrifuge tube in order. Then, the Si NP solution was carefully dropped on the sucrose solution and centrifuge at 4000 RCF for 90 min. The size-separated Si NP solutions were retrieved from the top to bottom of solution and transferred to water.^[56]

Silica coated Gold. The synthesis of Au@SiO₂ was realized using the method developed by Xue et al.^[61] Briefly, an ethanolic solution of MHA was added to commercially available 60nm AuNPs (BBI) to the final concentration of 20μM. This solution was then centrifuged at 5000g for 10 min and redispersed in a 0.1 ethanolic solution of TEOS. Finally, DMA (a 40% aqueous solution) was added while stirring until the DMA concentration reached 0.6 M. After 3 h of the SiO₂ deposition, the core-shell nanoparticles obtained were centrifuged twice for 10 min at 3000g and redispersed in ethanol. Core-shell NPs were dried overnight on a desiccator, for further functionalization with azide.

Titanium. Commercially available 150nm TiO₂NPs (Sigma Aldrich Prod. N: 914835) were dried overnight on a desiccator, for further functionalization with azide.

Azide modified oxides-rich nanoparticles. 2pmol of dried 150nm nanoparticles were dispersed in 10mL of DMF anhydrous by ultrasonication in an 20mL vial. 4μl of CPTMS was added and sonicated at 70°C for 2hs. NaN₃ was incorporated in excess and the mixture was stirred at 40°C overnight. The

nanoparticles were purified by centrifugation at 5000rcf for 5min and redispersion, twice in methanol and twice in water consecutively. ^[62]

Azide modified polymeric nanoparticles. 2uM azide modified PMMA and 5uM azide modified PS particles were purchase from PolyAn molecular surface engineering (Prod. N: 108 35 002) and Spherotech (Prod. N: ACCP-50-5) respectively.

Azide modified Gold nanoparticles. 500ul 60nm AuNPs OD1.5 were mixed with 14ul 200uM SH-PEG5-N3 and vortex for 5 seconds. Afterwards 10ul 10%SDS were added, and finger sonicated. To purify, the particles were centrifuge for 5min at 4000 rcf and resuspended in SDS 0.1

DNA functionalization of nanoparticles. 1mL 0.1wt% nanoparticles were centrifuged for 5 min at 5000rcf and resuspended in 300ul 100uM DBCO-modified DNA (Biomers GmbH). 1mL 1X PBS pH7.5 0.1% SDS was added to the mixture, which was then frozen at -20°C for 2 hours. The nanoparticles were thawed by sonication for 5 min before being centrifuged twice at 2000rcf for 10 min and resuspended in 50uL water. A 0.3wt% agarose (LE Agarose, Biozym Scientific GmbH) electrophoresis gel in TAE 0.5X (20 mM Tris, 5 mM Acetate, 0.5 mM EDTA) and 6mM MgCl₂ was run for 3 hs at 100eV to purify the nanoparticles and remove potential aggregates. The nanoparticles were recovered by squeezing the desired bands from the gel.

Particles analysis. At 25°C, an Anton Paar (Litesizer 500) Z-sizer device was used for Dynamic Light Scattering (DLS) and Electrophoretic Light Scattering (ELS) measurements. 5 repetitions (50 minutes each) and 3 repetitions for DLS and Z-Potential respectively were averaged, with the standard deviation respectively serving as the error bar. The Smoluchowski approximation was used as model for the Z-potential measurements.

Fluorescence spectroscopy was performed with a Horiba Fluorolog 3 spectrometer with right angle illumination equipped with a 450 W Xenon light source for excitation and a FL-1030-UP photomultiplier as detector. Measurements were carried out exciting at 530nm with a 3nm band pass and collecting with a 3nm band pass from 550-800nm and 1nm increment step.

CryoEM and EELS measurements were performed in CIME-EPFL facilities by the specialists Dr. Davide Demurtas and Dr. David F. Reyes Vasquez respectively.

Surface density quantification. DBCO-Cy5 was reacted with N₃-NPs, and the extinction spectra before (mix) and after (NPs) purification was measured to calculate Cy5 concentration (E_{650nm}) normalized by SiO₂ concentration (E_{350nm}) in each case. A ratio of Cy5/ NP was obtained and normalized by the surface of a sphere with the following formula.

$$Cy5 \left[\frac{cy5}{nm^2} \right] = \frac{E_{650nm}^{NPs} \cdot V^{NPs}}{E_{350nm}^{NPs}} \cdot \frac{E_{350nm}^{mix}}{E_{650nm}^{mix} \cdot V^i} \cdot C_{Cy5}^{mix} \cdot \frac{1}{4\pi r^2} \quad \text{eq. S1}$$

being C_{Cy5} the concentration of cy5, and r the radius of the NPs in nm. DNA surface density was calculated in an analog way by extinction at 260nm.

$$DNA \left[\frac{DNA}{nm^2} \right] = \frac{E_{260nm}^{NPs} \cdot V^{NPs}}{E_{350nm}^{NPs}} \cdot \frac{E_{350nm}^{mix}}{E_{260nm}^{mix} \cdot V^i} \cdot C_{DNA}^{mix} \cdot \frac{1}{4\pi r^2} \quad \text{eq. S2}$$

DNA origami synthesis. The rectangular DNA origami structure with a pillar in the center was designed using CaDNAno^[63]-accessible at <https://nanobase.org/structure/146>^[64]. A 7249- nucleotide long scaffold extracted from the M13mp18 bacteriophage (Bayou Biolabs LLC) was folded into the desired shape using 186 staples in 1x TAE (40 mM Tris, 10 mM Acetate, 1 mM EDTA), 12 mM MgCl₂, pH 8 buffer. It was mixed in a 10-fold excess of staples (IDT) over scaffold, and 100-fold for especially modified staples (Biomers GmbH). The mixture was heated to 70°C and cooled down on a rate of 1°C

every 20 min up to 25°C. The DNA origami structures were purified by 1wt% agarose (LE Agarose, Biozym Scientific GmbH) gel electrophoresis at 70V for 2 hours. [65]

DNA Origami mediated Dimers. N₃-NPs were functionalized with a 1 to 1 mix of DBCO-T28/-T18, purify as stated and mix ON with origami in a 1:10 (Origami : NPs) ratio. Samples were purified by 0.3wt% 0.5X TAE, 6mM Mg²⁺ agarose gel electrophoresis at 70V for 3hs. Desired bands were deposit on custom made Chromium grids coated with BSA-Biotin and Neutravidin via Biotin protrusions from the bottom of the Origami. Single molecule fluorescence measurements for the visualization of DNA origami structures containing single ATTO647N fluorophores were carried out on a custom-built widefield microscope [65,66] and later colocalize with the nanoparticles observed on a TESCAN Mira 3 field emission scanning electron microscope.

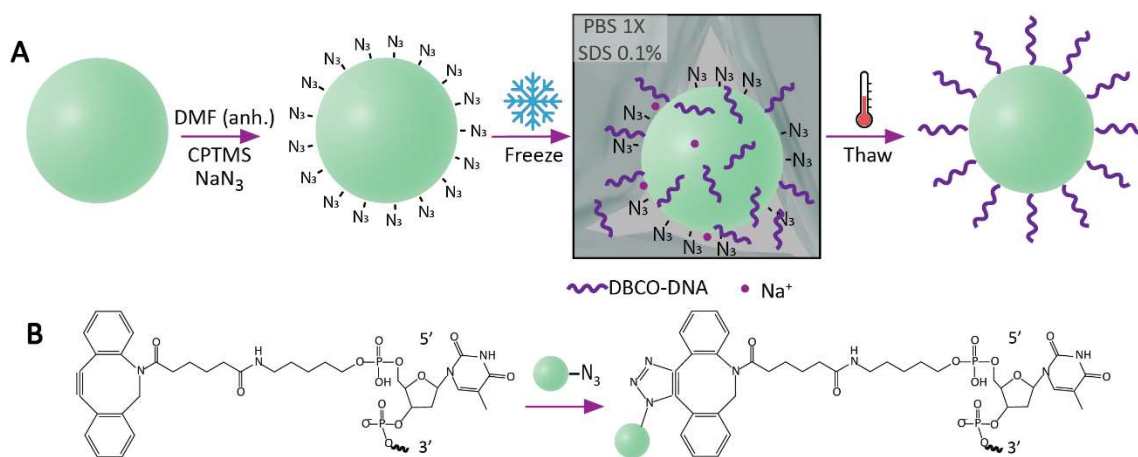


Figure 1: General Protocol. Two steps DNA grafting of oxide-rich NPs: Azide functionalization via CPTMS silanization and Chloro-Azide substitution, in DMF anhydrous, followed by freezing (freeze&thaw) assisted DBCO-DNA deposition (a) via strain promoted azide-alkyne cycloaddition (SPAAC) (b).

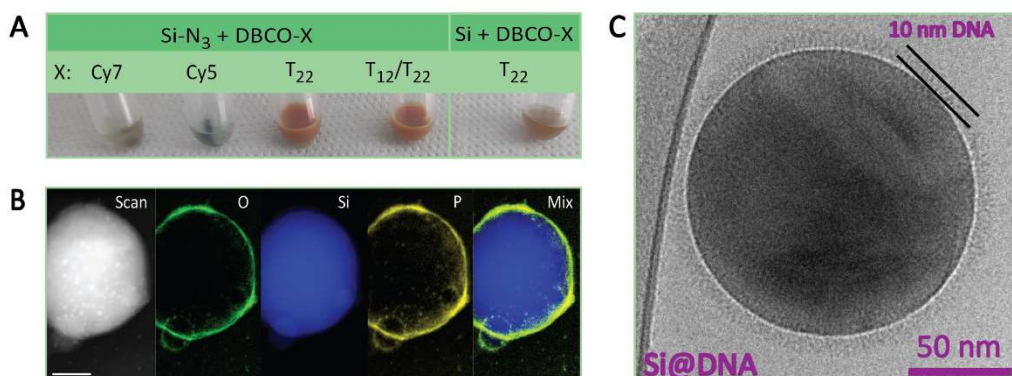


Figure 2: DNA functionalization of Si nanoparticles. Azide functionalized SiNPs after mixing with DBCO modified Cy5, Cy7, and DNA (both 100% 22-thyminins, T₂₂, and 50% mixed with 12-Thyminins, T₁₂/T₂₂) compared with Bare SiNPs reacted with DBCO-DNA (a). Analysis 140nm SiNP functionalized with T36 DNA by EELS showing the scan, oxygen (green), Silicon (blue), phosphorus (yellow), and their overlap (Mix), (b) and CryoEM pointing at the 10nm DNA shell (c). Scale bars are 50nm

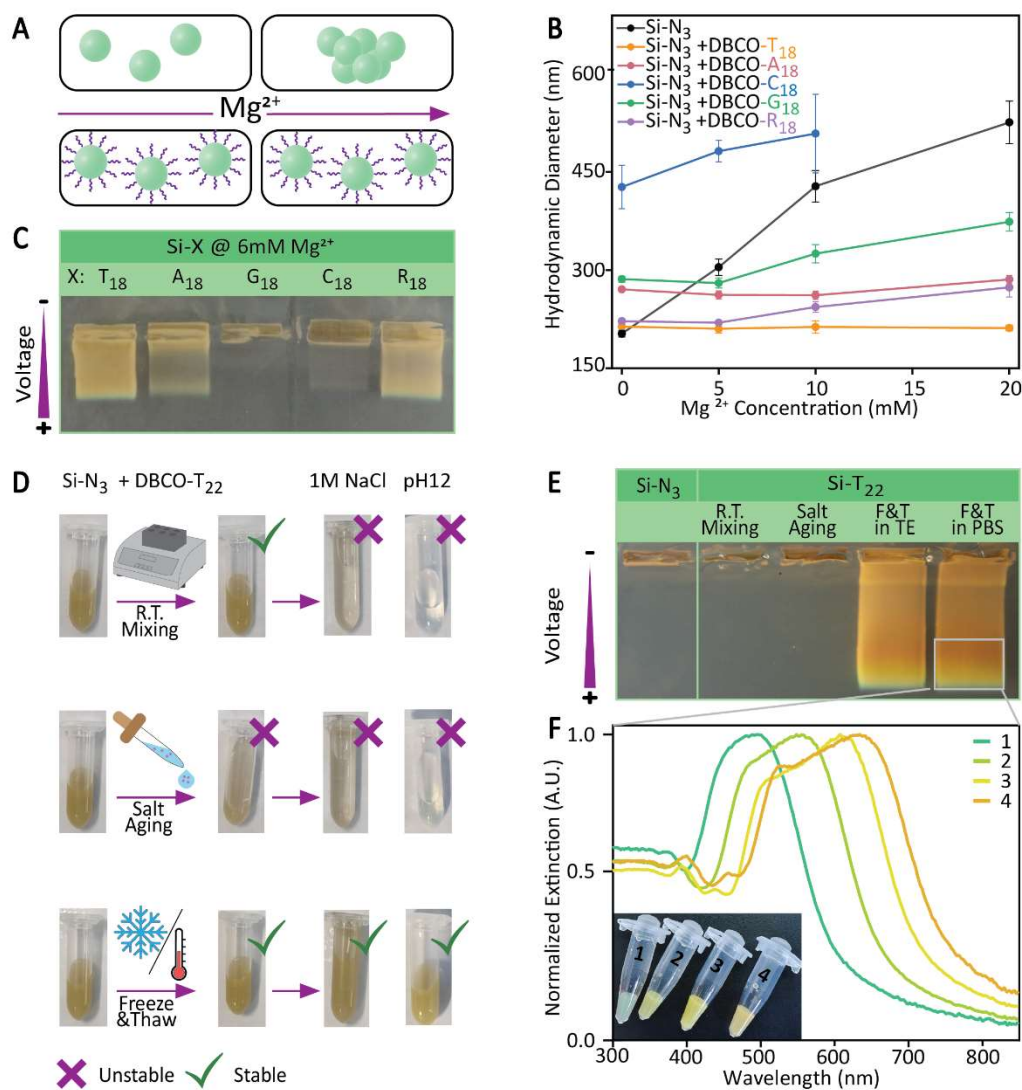


Figure3: Reaction Characterization. Stability scheme of SiNPs without (upper chart) and with (lower chart) DNA towards higher salt concentrations (a). DLS of SiNPs under different salt concentration for N₃ (black), T₁₈ (orange), A₁₈(pink), C₁₈(blue), G₁₈(green), R₁₈(violet). Lines are not a fit but guidelines (b), and the corresponding electrophoresis gel (c). Images of SiNPs before and after functionalization with DBCO DNA at R.T. mixing for 48hs, with Salt aging method, and by freeze and Thaw (F&T), and the images 10 min after adding 1M NaCl, or KOH till reaching pH12(d). Indicating stability (tick) and instability (cross) under the aforementioned procedures. Electrophoresis gel of Si-N3 NPs and DNA functionalized NPs with different methods: Mixer, SA, and F&T both in Tris-EDTA buffer (TE) and Phosphate buffer saline (PBS) (e). Normalized extinction spectra of electrophoresis size separated NPs with the insert showing each solution after cutting out from the gel (f). All gel electrophoresis were 0.3 wt% agarose in 0.5xTEA 6mM Mg²⁺.

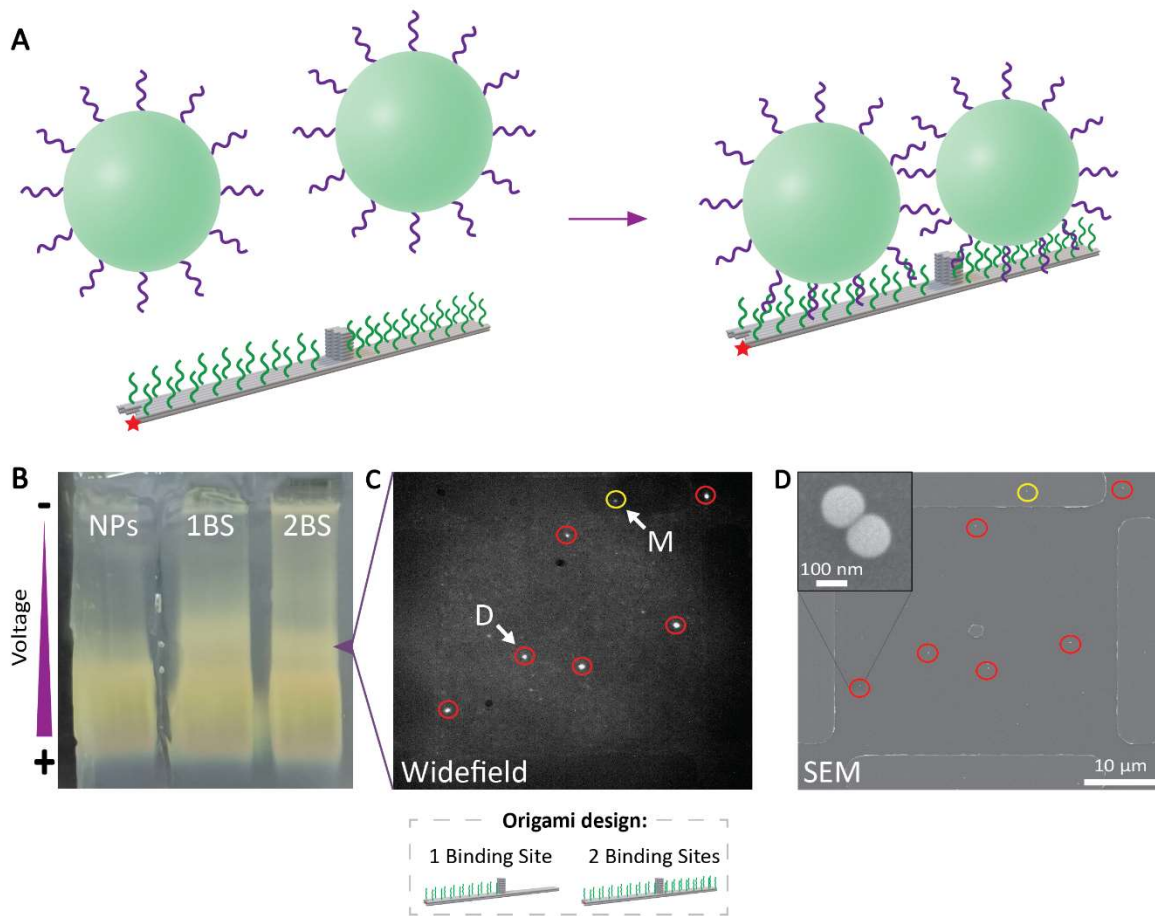


Figure 4: Assembly to DNA origami. Scheme of assembly between DNA-functionalized SiNPs and DNA origami structure (boat) with 2 lines of poly adenine (green protrusions) and Atto647N fluorophore (red dot) for the formation of Si-Dimers (a). Agarose Gel of dimer design structure (2BS), monomer design structure (1BS) and NPs indicating the band of interest with an arrow(b). WF (c) and SEM (d) colocalization of 2BS origami design showing dimers (red) and monomers (yellow). Insert shows a Magnification on one of the dimers.

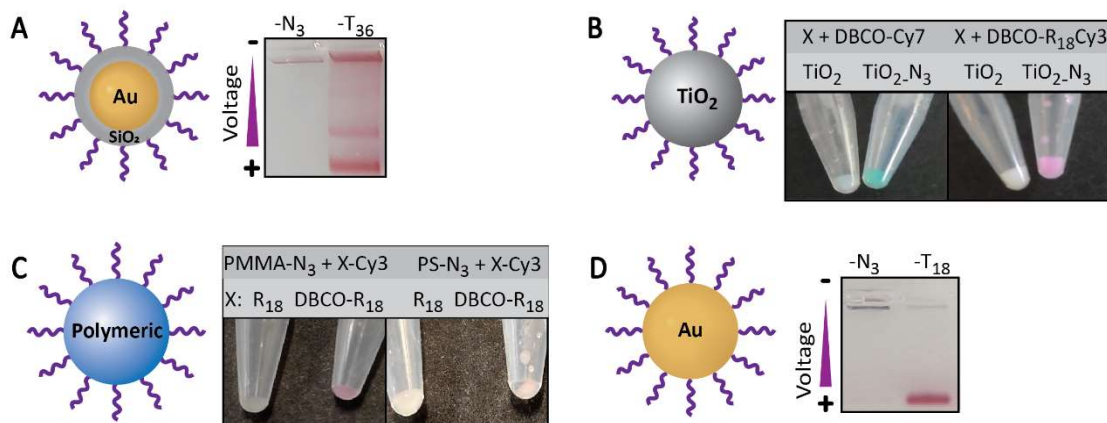


Figure5: Versatility of freezing assisted DBCO-N3. Agarose gel electrophoresis of 60nm Au@SiO₂ NPs before (N₃) and after (T₃₆) DNA functionalization (a). Images of TiO₂ (left) and TiO₂-N₃ (right) after reaction with DBCO-Cy7 (left chart) and with DBCO-R₁₈-Cy3 (right chart) (b). Images of commercially available N3 functionalized 2μm PMMA (left chart) and 5μm PS (right chart) NPs after reaction with DBCO-R₁₈-Cy3 and R₁₈-Cy3 (c). Agarose gel electrophoresis 60nm Au@SH-PEG₅-N₃ before (N₃) and after (T₁₈) DNA functionalization (d).

- [1] A. R. Tao, S. Habas, P. Yang, *Small* **2008**, *4*, 310.
- [2] A. Heuer-Jungemann, N. Feliu, I. Bakaimi, M. Hamaly, A. Alkilany, I. Chakraborty, A. Masood, M. F. Casula, A. Kostopoulou, E. Oh, K. Susumu, M. H. Stewart, I. L. Medintz, E. Stratakis, W. J. Parak, A. G. Kanaras, *Chem. Rev.* **2019**, *119*, 4819.
- [3] K. L. Kelly, E. Coronado, L. L. Zhao, G. C. Schatz, *J. Phys. Chem. B* **2003**, *107*, 668.
- [4] A. Lekawa-Raus, J. Patmore, L. Kurzepa, J. Bulmer, K. Koziol, *Adv. Funct. Mater.* **2014**, *24*, 3661.
- [5] Q. A. Pankhurst, J. Connolly, S. K. Jones, J. Dobson, *J. Phys. Appl. Phys.* **2003**, *36*, R167.
- [6] Q. Wu, W. Miao, Y. Zhang, H. Gao, D. Hui, *Nanotechnol. Rev.* **2020**, *9*, 259.
- [7] N. Joudeh, D. Linke, *J. Nanobiotechnology* **2022**, *20*, 262.
- [8] T. Chen, M. I. Shukoor, Y. Chen, Q. Yuan, Z. Zhu, Z. Zhao, B. Gulbakan, W. Tan, *Nanoscale* **2011**, *3*, 546.
- [9] H. T. Phan, A. J. Haes, *J. Phys. Chem. C Nanomater. Interfaces* **2019**, *123*, 16495.
- [10] B. Wang, X. He, Z. Zhang, Y. Zhao, W. Feng, *Acc. Chem. Res.* **2013**, *46*, 761.
- [11] D. A. Giljohann, D. S. Seferos, W. L. Daniel, M. D. Massich, P. C. Patel, C. A. Mirkin, *Angew. Chem. Int. Ed Engl.* **2010**, *49*, 3280.
- [12] L. Xu, H.-W. Liang, Y. Yang, S.-H. Yu, *Chem. Rev.* **2018**, *118*, 3209.
- [13] F. Lu, K. G. Yager, Y. Zhang, H. Xin, O. Gang, *Nat. Commun.* **2015**, *6*, 6912.
- [14] S. E. Seo, M. Girard, M. Olvera de la Cruz, C. A. Mirkin, *Nat. Commun.* **2018**, *9*, 4558.
- [15] T. Zhang, C. Hartl, K. Frank, A. Heuer-Jungemann, S. Fischer, P. C. Nickels, B. Nickel, T. Liedl, *Adv. Mater.* **2018**, *30*, 1800273.
- [16] H. Aldewachi, T. Chalati, M. N. Woodroffe, N. Bricklebank, B. Sharrack, P. Gardiner, *Nanoscale* **2017**, *10*, 18.
- [17] M. Dass, F. N. Gür, K. Kołataj, M. J. Urban, T. Liedl, *J. Phys. Chem. C* **2021**, *125*, 5969.
- [18] S. Siddique, J. C. L. Chow, *Appl. Sci.* **2020**, *10*, 3824.
- [19] C. A. Mirkin, R. L. Letsinger, R. C. Mucic, J. J. Storhoff, *Nature* **1996**, *382*, 607.
- [20] J. I. Cutler, E. Auyeung, C. A. Mirkin, *J. Am. Chem. Soc.* **2012**, *134*, 1376.
- [21] X. Zhang, M. R. Servos, J. Liu, *J. Am. Chem. Soc.* **2012**, *134*, 7266.
- [22] S. J. Hurst, A. K. R. Lytton-Jean, C. A. Mirkin, *Anal. Chem.* **2006**, *78*, 8313.
- [23] Y. Hao, Y. Li, L. Song, Z. Deng, *J. Am. Chem. Soc.* **2021**, *143*, 3065.
- [24] M. Huang, E. Xiong, Y. Wang, M. Hu, H. Yue, T. Tian, D. Zhu, H. Liu, X. Zhou, *Nat. Commun.* **2022**, *13*, 968.
- [25] B. Liu, J. Liu, *J. Am. Chem. Soc.* **2017**, *139*, 9471.
- [26] X. Zhang, M. R. Servos, J. Liu, *Chem. Commun.* **2012**, *48*, 10114.
- [27] Z. Qing, G. Luo, S. Xing, Z. Zou, Y. Lei, J. Liu, R. Yang, *Angew. Chem. Int. Ed.* **2020**, *59*, 14044.
- [28] "A Versatile Approach to the Synthesis of Functionalized Thiol-Protected Palladium Nanoparticles," DOI 10.1021/cm2014658 can be found under <https://pubs.acs.org/doi/epdf/10.1021/cm2014658>, **n.d.**

- [29] “Self-Assembled Monolayers of Thiolates on Metals as a Form of Nanotechnology | Chemical Reviews,” can be found under <https://pubs.acs.org/doi/10.1021/cr0300789>, **n.d.**
- [30] A. A. Nayl, A. I. Abd-Elhamid, A. A. Aly, S. Bräse, *RSC Adv.* **2022**, *12*, 13706.
- [31] J. Wang, Z. Wang, W. Wang, Y. Wang, X. Hu, J. Liu, X. Gong, W. Miao, L. Ding, X. Li, J. Tang, *Nanoscale* **2022**, *14*, 6709.
- [32] J. F. Li, Y. F. Huang, Y. Ding, Z. L. Yang, S. B. Li, X. S. Zhou, F. R. Fan, W. Zhang, Z. Y. Zhou, D. Y. Wu, B. Ren, Z. L. Wang, Z. Q. Tian, *Nature* **2010**, *464*, 392.
- [33] M. J. Mitchell, M. M. Billingsley, R. M. Haley, M. E. Wechsler, N. A. Peppas, R. Langer, *Nat. Rev. Drug Discov.* **2021**, *20*, 101.
- [34] T. Repenko, A. Rix, S. Ludwanowski, D. Go, F. Kiessling, W. Lederle, A. J. C. Kuehne, *Nat. Commun.* **2017**, *8*, 470.
- [35] J. M. Sanz, D. Ortiz, R. Alcaraz de la Osa, J. M. Saiz, F. González, A. S. Brown, M. Losurdo, H. O. Everitt, F. Moreno, *J. Phys. Chem. C* **2013**, *117*, 19606.
- [36] A. I. Barreda, J. M. Saiz, F. González, F. Moreno, P. Albella, *AIP Adv.* **2019**, *9*, 040701.
- [37] J. Hu, M. Lawrence, J. A. Dionne, *ACS Photonics* **2020**, *7*, 36.
- [38] C.-S. Ho, A. Garcia-Etxarri, Y. Zhao, J. Dionne, *ACS Photonics* **2017**, *4*, 197.
- [39] Y. H. Fu, A. I. Kuznetsov, A. E. Miroshnichenko, Y. F. Yu, B. Luk'yanchuk, *Nat. Commun.* **2013**, *4*, 1527.
- [40] A. Matsumori, H. Sugimoto, M. Fujii, *Laser Photonics Rev.* **2023**, *17*, 2300314.
- [41] A. Vaskin, S. Mashhadi, M. Steinert, K. E. Chong, D. Keene, S. Nanz, A. Abass, E. Rusak, D.-Y. Choi, I. Fernandez-Corbaton, T. Pertsch, C. Rockstuhl, M. A. Noginov, Y. S. Kivshar, D. N. Neshev, N. Noginova, I. Staude, *Nano Lett.* **2019**, *19*, 1015.
- [42] M. K. Schmidt, R. Esteban, J. J. Sáenz, I. Suárez-Lacalle, S. Mackowski, J. Aizpurua, *Opt. Express* **2012**, *20*, 13636.
- [43] Y. Wang, Y. Wang, X. Zheng, É. Ducrot, M. G. Lee, G. R. Yi, M. Weck, D. J. Pine, *J. Am. Chem. Soc.* **2015**, *137*, 10760.
- [44] Y. Wang, Y. Wang, X. Zheng, É. Ducrot, J. S. Yodh, M. Weck, D. J. Pine, *Nat. Commun.* **2015**, *6*, 7253.
- [45] M. He, J. P. Gales, É. Ducrot, Z. Gong, G.-R. Yi, S. Sacanna, D. J. Pine, *Nature* **2020**, *585*, 524.
- [46] A. Lak, Y. Wang, P. J. Kolbeck, C. Pauer, M. S. Chowdhury, M. Cassani, F. Ludwig, T. Viereck, F. Selbach, P. Tinnefeld, M. Schilling, T. Liedl, J. Tavaoli, J. Lipfert, **2023**.
- [47] S. Mushtaq, S.-J. Yun, J. Jeon, *Molecules* **2019**, *24*, 3567.
- [48] G. Yi, J. Son, J. Yoo, C. Park, H. Koo, *Biomater. Res.* **2018**, *22*, 13.
- [49] Y. Ye, S. Hou, X. Wu, X. Cheng, S. He, *Langmuir* **2022**, *38*, 4625.
- [50] S. V. German, M. V. Novoselova, D. N. Bratashov, P. A. Demina, V. S. Atkin, D. V. Voronin, B. N. Khlebtsov, B. V. Parakhonskiy, G. B. Sukhorukov, D. A. Gorin, *Sci. Rep.* **2018**, *8*, 17763.
- [51] F. Vargas-Lara, F. W. Starr, J. F. Douglas, *Nanoscale Adv.* **2022**, *4*, 4144.
- [52] J. F. Douglas, F. W. Starr, F. Vargas-Lara, Naples, Italy, **2016**, p. 020081.
- [53] X. Zhang, M. R. Servos, J. Liu, *J. Am. Chem. Soc.* **2012**, *134*, 9910.
- [54] Z.-S. Wu, M.-M. Guo, G.-L. Shen, R.-Q. Yu, *Anal. Bioanal. Chem.* **2007**, *387*, 2623.
- [55] D. Zhu, J. Chao, H. Pei, X. Zuo, Q. Huang, L. Wang, W. Huang, C. Fan, *ACS Appl. Mater. Interfaces* **2015**, *7*, 11047.
- [56] H. Sugimoto, T. Okazaki, M. Fujii, *Adv. Opt. Mater.* **2020**, *8*, 2000033.
- [57] C.-Y. Li, S. Duan, J. Yi, C. Wang, P. M. Radjenovic, Z.-Q. Tian, J.-F. Li, *Sci. Adv.* **2020**, *6*, eaba6012.
- [58] H.-K. Choi, K. S. Lee, H.-H. Shin, J.-J. Koo, G. J. Yeon, Z. H. Kim, *Acc. Chem. Res.* **2019**, *52*, 3008.

- [59] K. Trofymchuk, K. Kołataj, V. Glembockyte, F. Zhu, G. P. Acuna, T. Liedl, P. Tinnefeld, *ACS Nano* **2023**, *17*, 1327.
- [60] W. Stöber, A. Fink, E. Bohn, *J. Colloid Interface Sci.* **1968**, *26*, 62.
- [61] C. Xue, X. Chen, S. J. Hurst, C. A. Mirkin, *Adv. Mater.* **2007**, *19*, 4071.
- [62] J. Chen, M. Liu, C. Chen, H. Gong, C. Gao, *ACS Appl. Mater. Interfaces* **2011**, *3*, 3215.
- [63] S. M. Douglas, A. H. Marblestone, S. Teerapittayanon, A. Vazquez, G. M. Church, W. M. Shih, *Nucleic Acids Res.* **2009**, *37*, 5001.
- [64] E. Poppleton, A. Mallya, S. Dey, J. Joseph, P. Šulc, *Nucleic Acids Res.* **2022**, *50*, D246.
- [65] C. Zaza, G. Chiarelli, L. P. Zweifel, M. Pilo-Pais, E. Sisamakias, F. Barachati, F. D. Stefani, G. P. Acuna, *Small Methods* **2023**, 2201565.
- [66] A. K. Adamczyk, T. A. P. M. Huijben, M. Sison, A. Di Luca, G. Chiarelli, S. Vanni, S. Brasselet, K. I. Mortensen, F. D. Stefani, M. Pilo-Pais, G. P. Acuna, *ACS Nano* **2022**, *16*, 16924.

Supplementary Figures

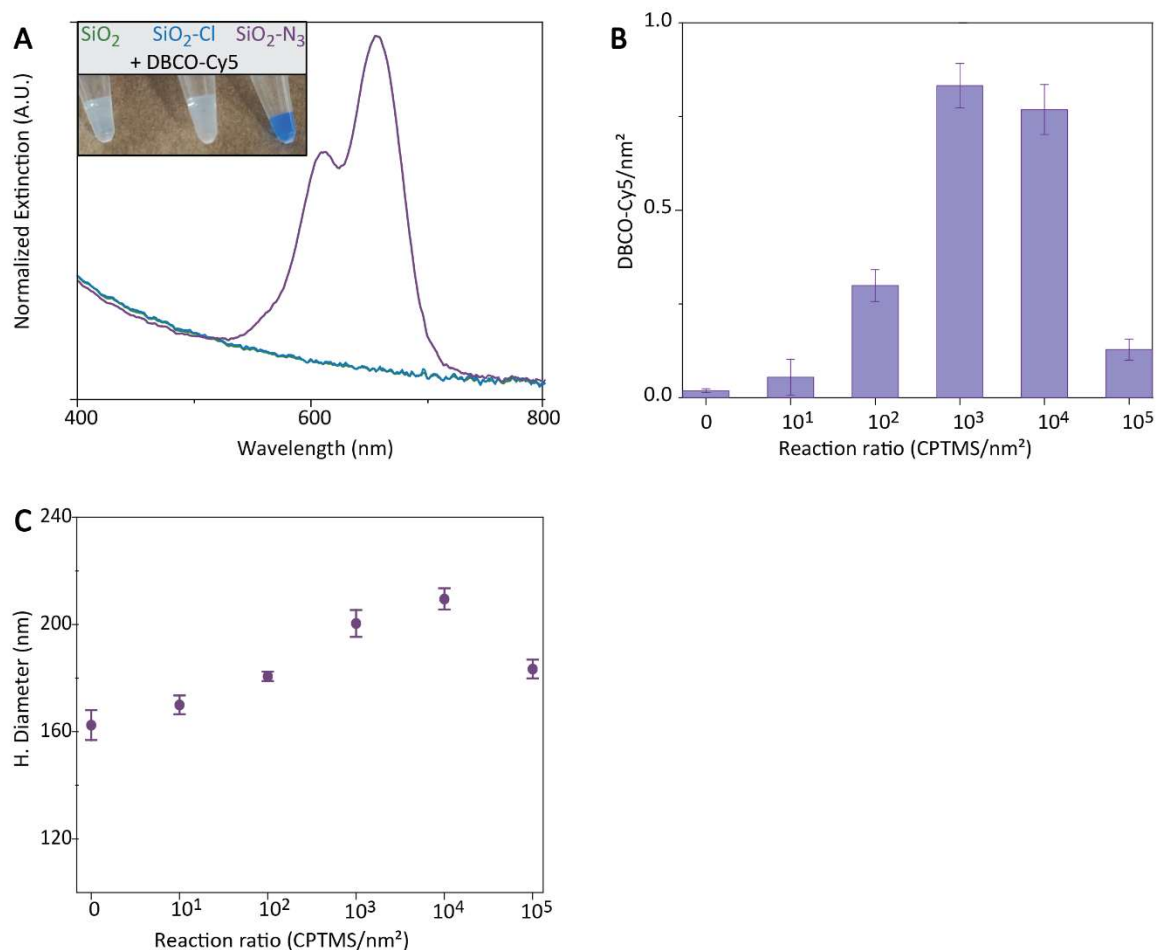


Figure S1: azide functionalization of SiO₂NPs. Extinction spectra and image (insert) of SiO₂ (green) SiO₂-Cl (bleu) and SiO₂-N₃ (violet) after reaction with DBCO-Cy5(a). Surface density for different CPTMS/SiO₂NPs reaction ratio(b) and corresponding hydrodynamic diameter measurements (c).

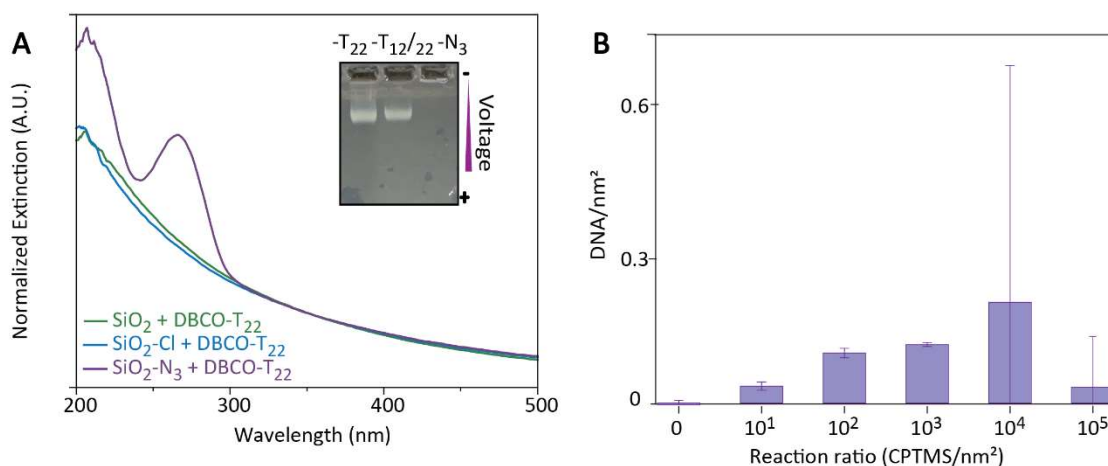


Figure S2: DNA functionalization of SiO₂NPs. Extinction spectra of SiO₂ (green) SiO₂-Cl (bleu) and SiO₂-N₃ (violet) after reaction with DBCO-T₂₂, and electrophoresis gel (insert) SiO₂-DNA NPs both 100% 22-thymins, T₂₂, and 50% mixed with 12-Thymims, T₁₂/T₂₂, and SiO₂-N₃ (a). DNA surface density for different CPTMS/SiO₂NPs reaction ratio (b).

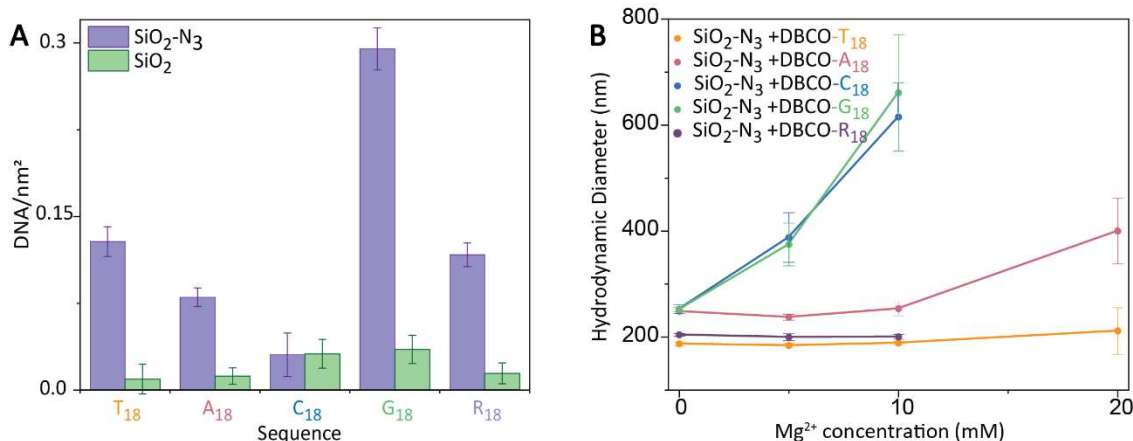


Figure S3: Sequence dependent DNA functionalization of SiO₂NPs. Surface density of SiO₂ (green) and SiO₂-N₃ after reaction with T₁₈ (orange), A₁₈(pink), C₁₈(blue), G₁₈(green), R₁₈(violet) (a), and corresponding DLS under different salt concentration (b) Lines are for eye guidance.

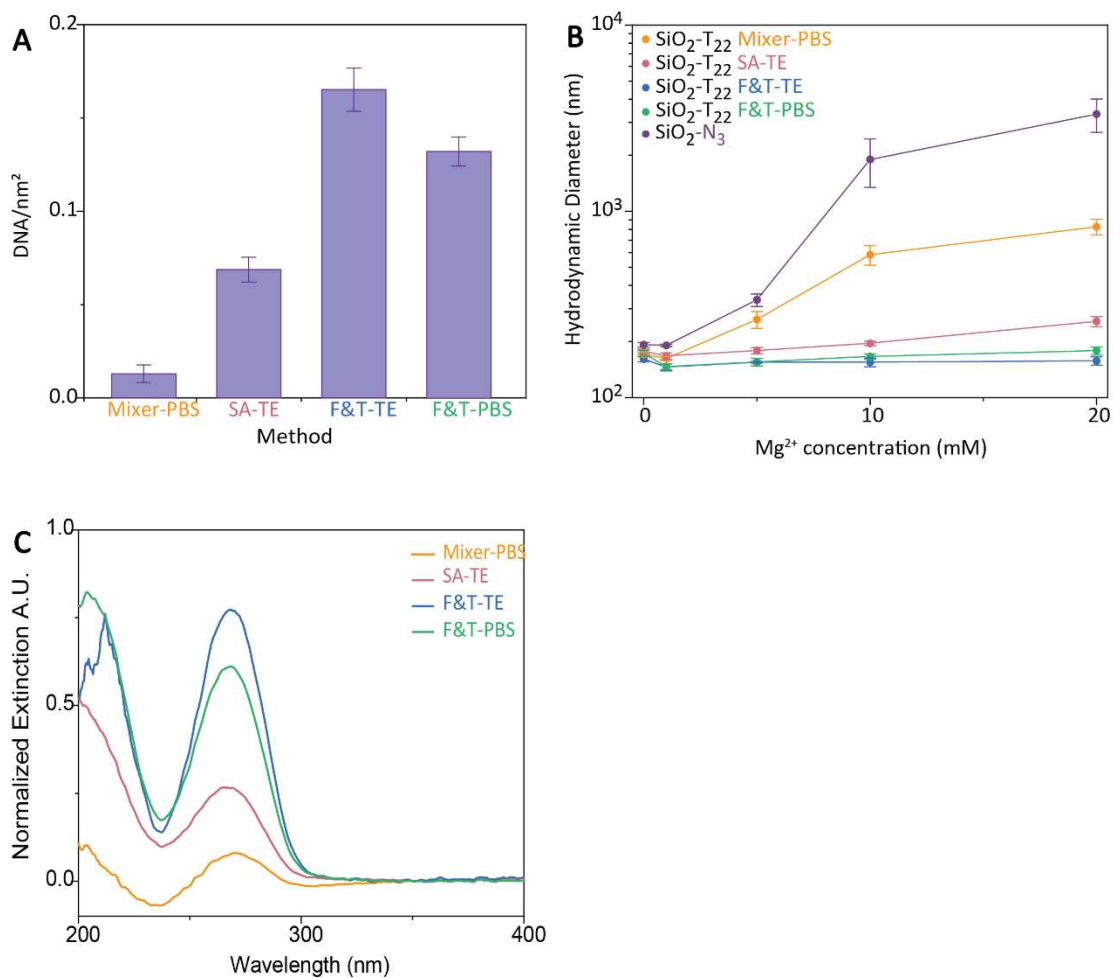


Figure S4: Method dependent DNA functionalization of SiO₂ NPs. Surface density of SiO₂-T₂₂ after reaction at RT mixing for 48hs (orange), with SA (pink), and by F&T method both in TE (blue) and PBS (green) (a), and corresponding DLS under different salt concentration (b). Lines are for eye guidance. Normalized Extinction spectra for the aforementioned methods (c)

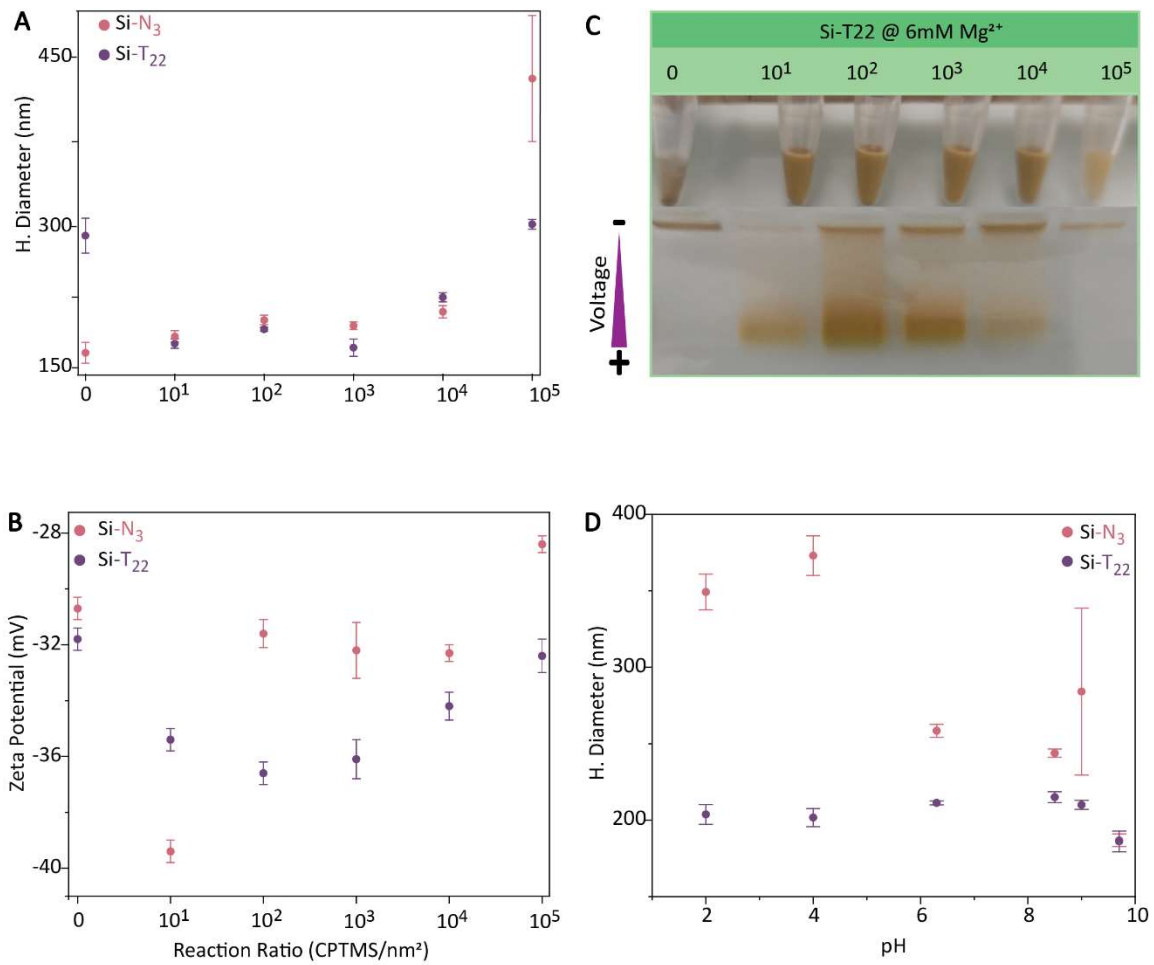


Figure S5: Functionalization of SiNPs. DLS (a) and Zeta potential (b) of N₃ (pink) and T₂₂ (violet) functionalized SiNPs for different CPTMS/nm² reaction ratio. Image and Agarose gel electrophoresis of Si-T₂₂ for different CPTMS/nm² reaction ratio (c). DLS of N₃ (pink) and T₂₂ (violet) under different pH(e).

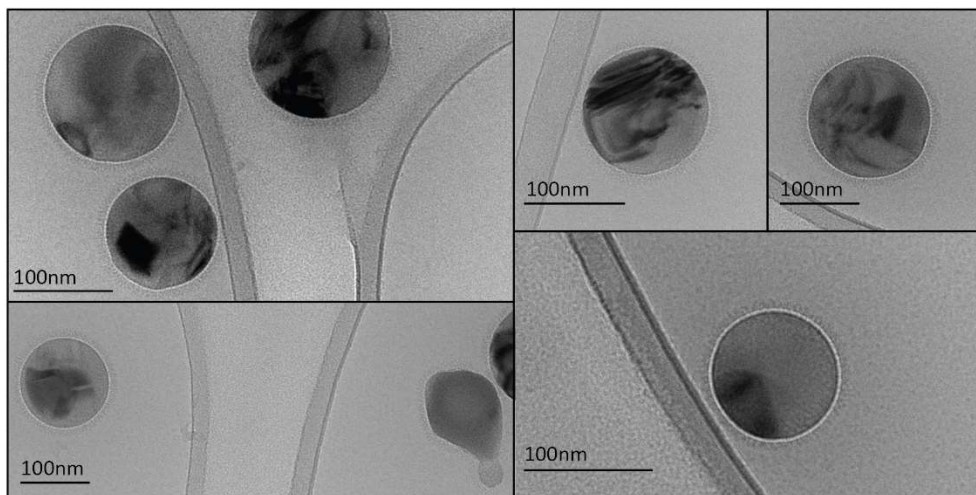


Figure S6: Imaging of Si-DNA NPs. Cryo EM Images of DNA functionalized 140nm Si NPs

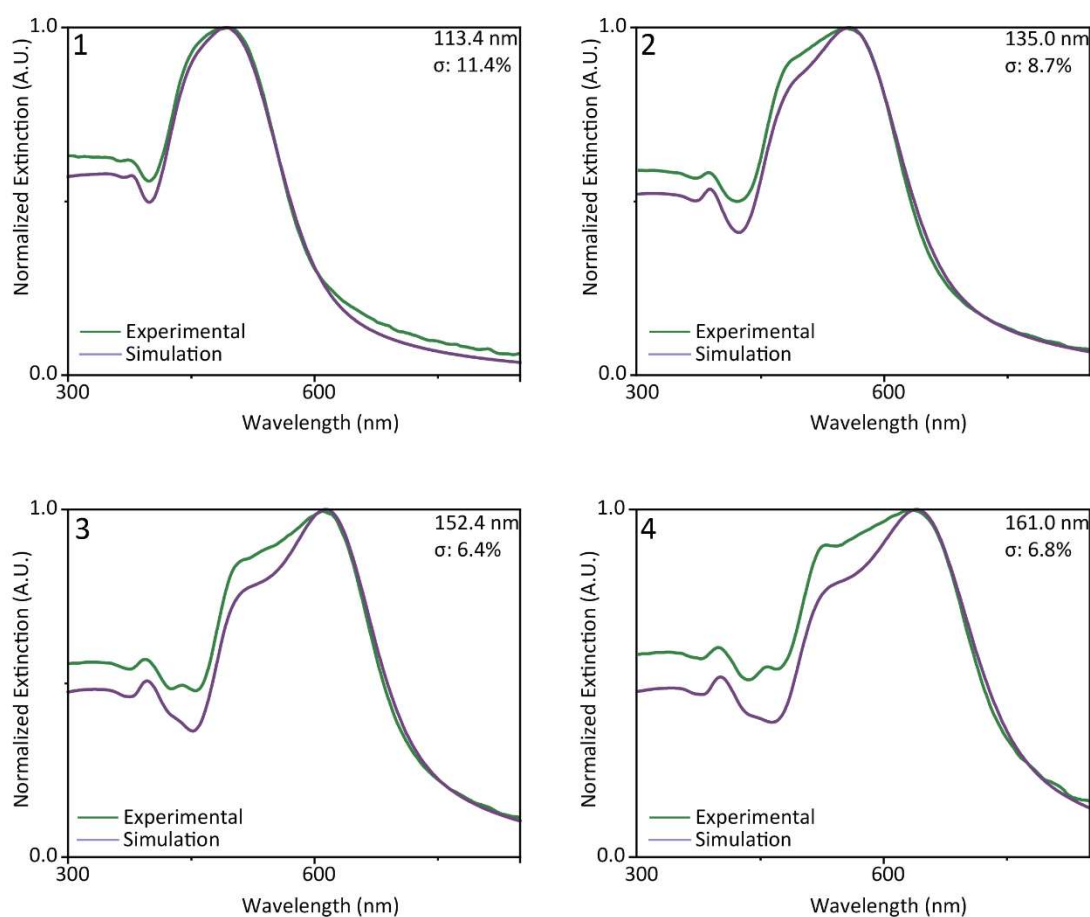


Figure S7: Size separation of Si NPs. Extinction Spectra measured (green) and simulated (violet) by Mie Theory of electrophoresis size separated SiNPs for their average size and size dispersion calculation.

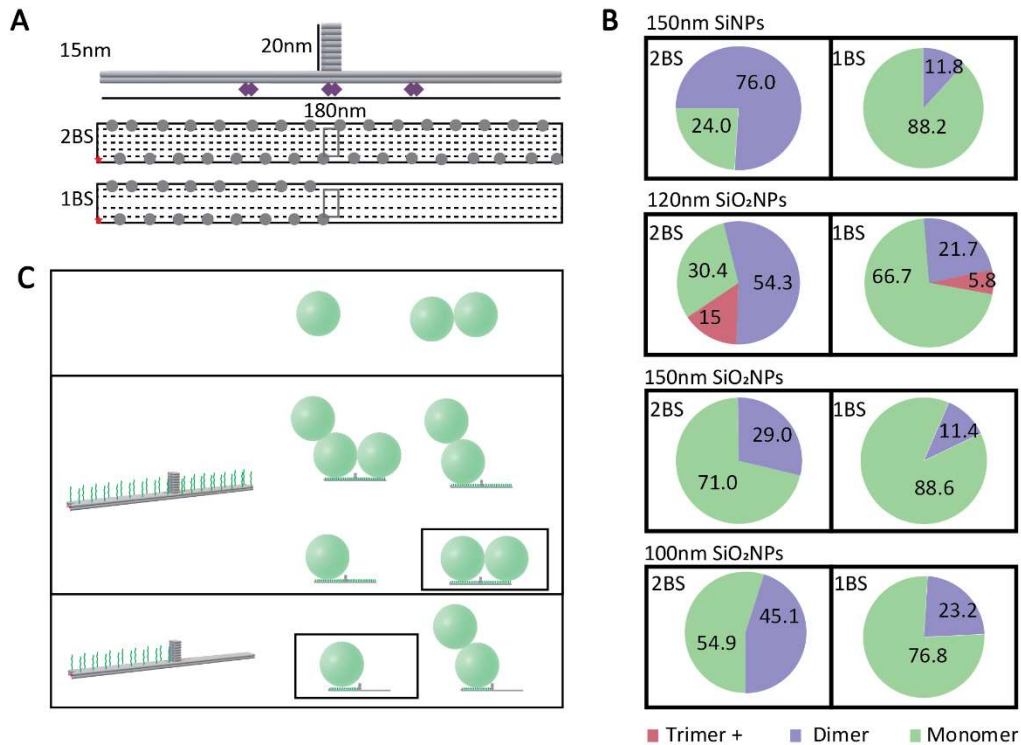


Figure S8: Assembly with DNA-origami. Scheme of origami design for Dimer (2BS) and Monomer (1BS) structures, with 2 lines of poly A extensions (green dots), the fluorophore ATTO 647N (red dot) and 6 biotins (violet diamonds) on the bottom for surface binding (a). Possible structures obtained after mixing SiNPs with preexisting dimerization with 2BS and 1BS structure. The desired structures are boxed (b). Statistics after WF SEM colocalization. Percentage of monomers in green, dimers in violet and higher order structures in pink for both 2BS (left) and 1BS (right) structures after assembly with: 150nm (upper chart) and 100nm (lower chart) SiNPs (c); and 150 nm (upper chart) and 100 nm (lower chart) SiO₂NPs (d).

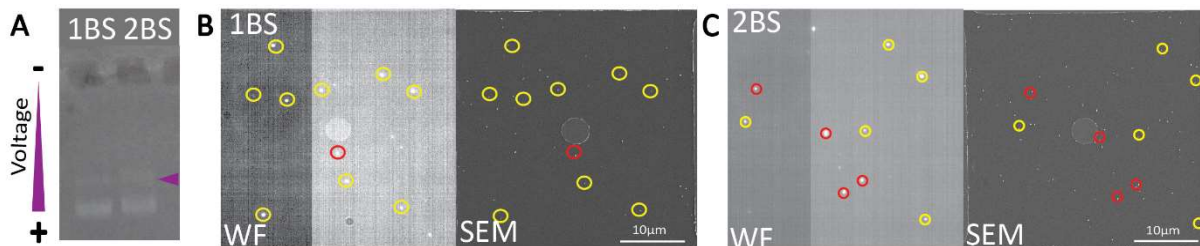


Figure S9: SiO₂ Dimers. Agarose Gel of dimer design structure (2BS), monomer design structure (1BS) and NPs indicating the band of interest with an arrow (b). WF and SEM colocalization of SiO₂NPs bound to 1BS (b) and 2BS (c) origami designs showing dimers (red) and monomers (yellow).

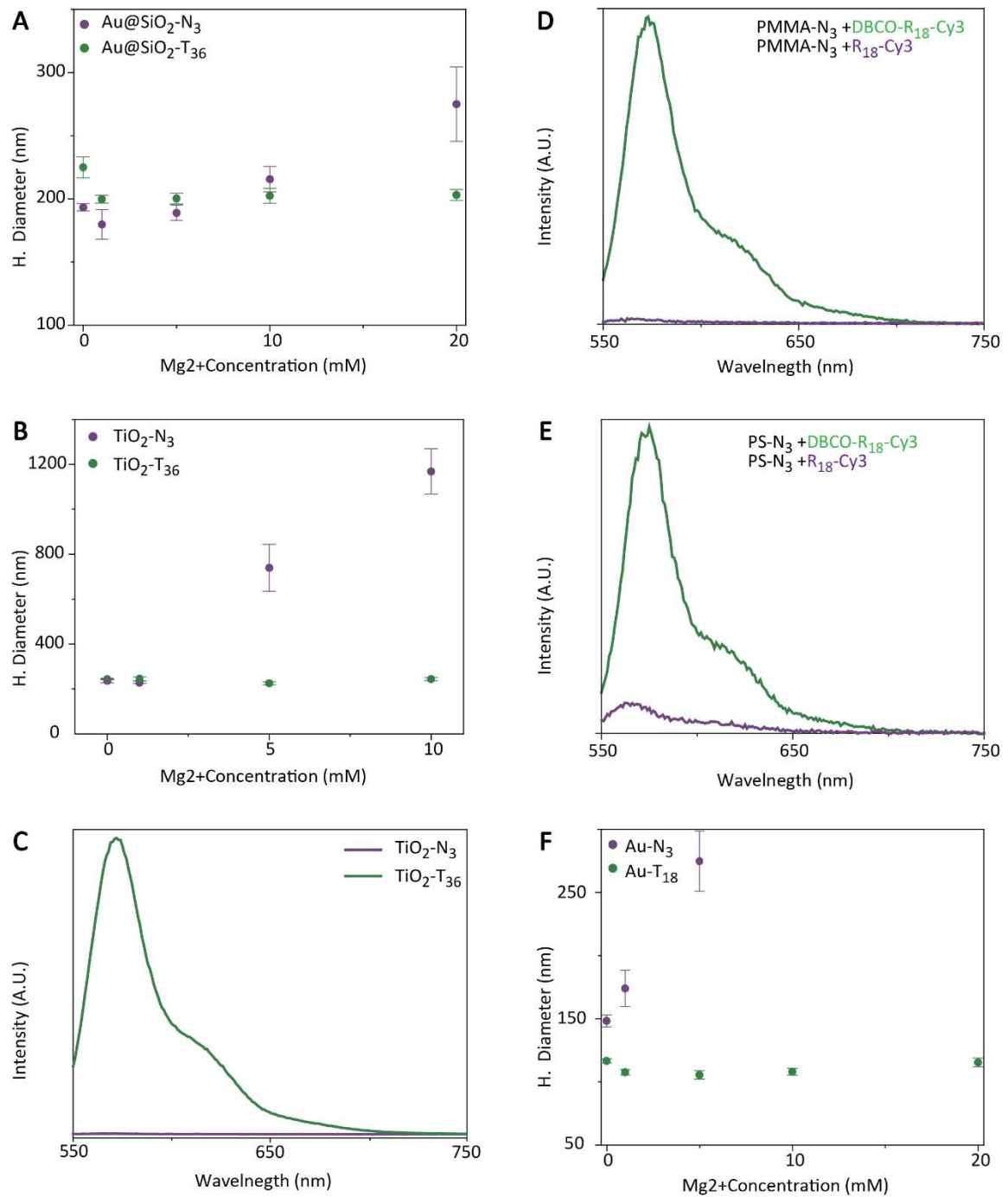


Figure S10 Versatility of freezing assisted DBCO azide reaction. DLS of Au@SiO₂ (a) and TiO₂(b) under different salt concentrations before (N3) and after (T36) DNA functionalization. Emission spectra of TiO₂(c) PMMA (d) and PS (e) after reaction with DBCO-R18-Cy3 (green) and R18-Cy3(violet). DLS of Au NPs before (N3) and after (T18) DNA functionalization under different salt concentrations